Inorganic Chemistry

Article

pubs.acs.org/IC

Complex 5d Magnetism in a Novel S = 1/2 Trimer System, the 12L Hexagonal Perovskite $Ba_4BiIr_3O_{12}$

Wojciech Miiller,[†,‡,§] Matthew T. Dunstan,[†,⊥] Zixin Huang,[†] Zakiah Mohamed,[†] Brendan J. Kennedy,[†] Maxim Avdeev,[‡] and Chris D. Ling*[,†]

[†]School of Chemistry, The University of Sydney, Sydney 2006, Australia

[‡]The Bragg Institute, ANSTO, PMB 1, Menai 2234, Australia

Supporting Information

ABSTRACT: The 12L hexagonal perovskite $Ba_4BiIr_3O_{12}$ has been synthesized for the first time and characterized using high-resolution neutron and synchrotron X-ray diffraction as well as physical properties measurements. The structure contains Ir_3O_{12} linear face-sharing octahedral trimer units, bridged by corner-sharing BiO_6 octahedra. The average electronic configurations of Ir and Bi are shown to be +4(d^5) and +4(s^1), respectively, the same as for the S = 1/2 dimer system $Ba_3BiIr_2O_9$, which undergoes a spin-gap opening with a strong magnetoelastic effect at T^* = 74 K. Anomalies in magnetic susceptibility, heat capacity, electrical resistivity, and unit cell parameters indeed reveal an analogous effect at $T^* \approx 215$ K in $Ba_4BiIr_3O_{12}$. However, the transition is not accompanied by the opening of a gap in spin excitation spectrum, because antiferromagnetic coupling among S = 1/2 Ir^{4+} (d^5) cations leads to the formation of a S = 1/2 doublet within the trimers, vs S = 0 singlets within dimers. The change in magnetic state of the trimers at T^* leads to a structural distortion, the energy of which is overcompensated for by the formation of S = 1/2 doublets. Extending this insight to the dimer system $Ba_3BiIr_2O_9$ sheds new light on the more pronounced low-temperature anomalies observed for that compound.

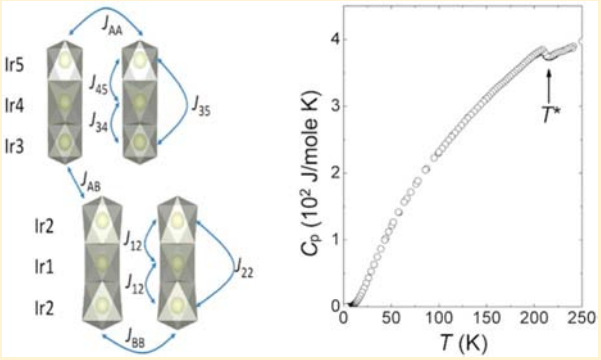

INTRODUCTION

Systems that exhibit quantum cooperative phenomena due to coupling between magnetic, electronic, and orbital degrees of freedom have attracted a great deal of interest in recent years.[1] An interesting class of quantum cooperative system is the low-dimensional antiferromagnetic (AFM) dimer systems, where interactions between neighboring electronic spins result in a gap opening between the singlet ground state and the excited triplet state.[2] Examples include $TlCuCl_3$,[3] $Ba_3Cr_2O_8$,[4] $CuIr_2S_4$,[5] and most recently, $Ba_3BiRu_2O_9$[6] and $Ba_3BiIr_2O_9$.[7] The spin-gap openings at T^* = 176 and 74 K, respectively, in these last two phases are accompanied by a large negative thermal volume expansion (1% in the case of $Ba_3BiIr_2O_9$), in a remarkably strong magnetoelastic coupling effect.

$Ba_3BiRu_2O_9$ and $Ba_3BiIr_2O_9$[8,9] are members of an isostructural series of 6H-type hexagonal perovskites $Ba_3RRu_2O_9$ or $Ba_3RIr_2O_9$ (R = Y, rare earth).[10−14] In the R = lanthanoid phases, magnetic properties are mostly associated with 4f ions. 6H-type perovskites consist of face-sharing bioctahedral M_2O_9 dimers that share vertices with RO_6 octahedra, with high-coordinate Ba^{2+} cations on the A sites. Direct M−M distances within the M_2O_9 dimers are relatively short at ∼2.5 Å, allowing for the possibility of direct metal−metal bonding. The oxidation states of M and R are coupled, with $R^{3+}/M^{4.5+}$ and R^{4+}/M^{4+} being the most common combination (R^{4+}/M^{4+} typically has the smaller unit cell). The unit cell volumes of $Ba_3BiRu_2O_9$ and $Ba_3BiIr_2O_9$ are comparable to other B^{4+}/M^{4+} 6H-type perovskites, suggesting that the oxidation state of Bi is +4.

Bi^{4+}, a highly unusual oxidation state, corresponding to an unstable $[Xe]4f^{14}5d^{10}6s^1$ electronic configuration, and is seldom observed in the solid state; nominally Bi^{4+} oxides normally disproportionate into Bi^{3+}/Bi^{5+}, as has been shown to occur in, for example, $BaBiO_3$.[15−20] However, in the case of $Ba_3BiRu_2O_9$ and $Ba_3BiIr_2O_9$, we could find no evidence for Bi^{3+}/Bi^{5+} disproportionation in our detailed high-resolution neutron and synchrotron X-ray diffraction studies, either above or below their magnetoelastic spin-gap transitions at T^*. We also saw no evidence for local disproportionation (peak broadening or anisotropic atomic displacement parameters), noting that BiO_6 octahedra are distributed on a pseudohexagonal lattice that could frustrate long-range ordering, or for charge transfer from Bi to M (i.e., $Bi^{4+}/M^{4+} \rightarrow Bi^{3+}/M^{4.5+}$). Considering that no spin-gap or structural transition is observed for any other $Ba_3RRu_2O_9$ or $Ba_3RIr_2O_9$ compound, it is reasonable to conclude that Bi in this unusual and unstable oxidation state plays a crucial role in the magnetoelastic spin-gap transitions. However, the exact mechanism remains unclear.

Received: June 10, 2013
Published: October 21, 2013

   dx.doi.org/10.1021/ic4014619 | Inorg. Chem. 2013, 52, 12461−12467

To shed more light on this, in the present study we investigated an analogue to $Ba_3BiIr_2O_9$ featuring Ir_3O_{12} face-sharing octahedral trimers in place of Ir_2O_9 dimers. The series of 12L-type hexagonal perovskites $Ba_4RRu_3O_{12}$ and $Ba_4RIr_3O_{12}$ had been reported for a wide range of R = lanthanoid[21−25] but not for R = Bi. We were unable to prepare $Ba_4BiRu_3O_{12}$, but we did succeed in producing high-quality samples of $Ba_4BiIr_3O_{12}$ for the first time. $Ba_4BiIr_3O_{12}$ shows evidence for a transition at ∼215 K analogous to that observed in $Ba_3BiIr_2O_9$, but it is orders of magnitude weaker in terms of both the magnetic and structural effects. The results help narrow down the possible mechanisms for these transitions by distinguishing the roles of Ir−Ir direct bonding and Bi^{4+} instability.

EXPERIMENTAL SECTION

Pure polycrystalline samples of 12L perovskite-type $Ba_4BiIr_3O_{12}$ were prepared by conventional solid-state reaction in air from $BaCO_3$, Bi_2O_3, and Ir metal (99.99% purity or greater). Prior to weighing, $BaCO_3$ was dried at 1000 K overnight. The stoichiometric mixture with a 10% excess of Bi_2O_3 was ground with an agate mortar and pestle, made into pellets and calcined at 873 K for 16 h. The sample was then reground, pelleted, and calcined at 1173 K for 48 h. Reaction progress and sample purity were monitored by conventional X-ray powder diffraction (XRD) collected on a Panalytical X'Pert Pro diffractometer using nonmonochromated Cu K_α radiation. Attempts to prepare the Ru analogue $Ba_4BiRu_3O_{12}$ by the same method (using both RuO_2 and Ru metal as reagents) were unsuccessful, instead producing a mixture of the dimer $Ba_3BiRu_2O_9$ and $BaRuO_3$.

Room-temperature time-of-flight neutron powder diffraction (NPD) data were collected on the HRPD instrument at the ISIS facility, U.K. The sample was placed in a 4 mm diameter vanadium can. Variable-temperature NPD data were collected on the instrument Echidna at the OPAL reactor (ANSTO, Lucas Heights, Australia) between 3 and 350 K at a wavelength of λ = 2.4395 Å. The sample was placed in a 6 mm diameter vanadium can and data collected in a closed-cycle cryofurnace.Low-temperature synchrotron XRD (S-XRD) data were collected at the Powder Diffraction (PD) beamline of the Australian Synchrotron between 130 and 250 K at a wavelength of λ = 0.824 60 Å (calibrated against a LaB_6 standard). Samples were placed in unsealed 0.3 mm diameter quartz capillaries, which were cooled in a liquid nitrogen cryostream.

Rietveld refinements against NPD data were carried out using the GSAS[26] program with the EXPGUI[27] front-end. Scale factors, zero shifts, background functions, and a single Lorentzian broadening term on top of the standard pseudo-Voigt peak shape functions for the instruments were refined. Data from the HRPD backscattering bank was used to refine structural parameters, which are presented in Table 1. Atomic displacement parameters (ADPs) were constrained to be equal for atoms of the same species. Metal−oxygen and short metal−metal bond lengths are presented in Table 2. The final Rietveld fit is shown in Figure 1 and the structure in Figure 2. The corresponding CIF file is available as deposited data.

Rietveld refinements against low-temperature S-XRD data were also carried out using GSAS and EXPGUI. Due to the relatively poor sensitivity of the X-ray data to light oxygen atoms in the presence of heavy Ba, Bi, and Ir atoms, it was not possible to reliably refine their structural parameters. We therefore used the model refined against NPD (HRPD, ISIS) data and refined only lattice parameters in addition to a scale factor, zero-shift, background function, and a single Lorentzian broadening term on top of the standard pseudo-Voigt peak shape function for the instrument. The final Rietveld fit to 250 K data (i.e., above the transition) is shown in Figure 3.

The temperature dependence of the lattice parameters obtained by Rietveld refinement between 3 and 350 K is shown in Figure 4. Data points from 130 to 250 K are from S-XRD data (highest resolution); other data points are from NPD (Echidna, OPAL).

Physical properties (magnetic susceptibility and heat capacity) were measured using a Quantum Design PPMS. Magnetic susceptibility data (Figure 5) were collected from 350 to 2 K in an applied magnetic field of 50 kOe using the vibrating sample magnetometer (VSM) technique. Unfortunately, it was not possible to collect useful data in lower fields due to the magnetically sparse nature of the system combined with the relatively high molar mass. For the same reason, attempts to collect useful ac-susceptibility measurements were unsuccessful.

Table 1. Structural Parameters and Bond Valence Sums[28] (BVS) for $Ba_4BiIr_3O_{12}$ at Room Temperature Refined against NPD (HRPD, ISIS) Data[a]

atom	x (a)	y (b)	z (c)	U_{iso} (100 Å^2)	BVS
Ba1	0.3356(2)	0	0.5391(7)	0.58(9)	1.66
Ba2	0.3500(2)	0	0.3794(6)	0.58(9)	2.03
Ba3	0.0023(2)	0	0.2820(7)	0.58(9)	1.98
Ba4	0.3295(2)	0	0.7993(6)	0.58(9)	2.01
Ba5	0.0096(2)	0	0.1266(7)	0.58(9)	2.18
Ba6	0.3224(2)	0	0.9480(7)	0.58(9)	2.01
Bi1	0.3328(18)	0	0.6695(5)	0.90(10)	3.69
Bi2	0	0	0	0.90(10)	3.56
Ir1	0	0	0.500000	0.73(6)	4.08
Ir2	0.0144(14)	0	0.4121(4)	0.73(6)	5.12
Ir3	0.3193(14)	0	0.2505(4)	0.73(6)	4.59
Ir4	0.3387(13)	0	0.1675(4)	0.73(6)	4.66
Ir5	0.3506(12)	0	0.0792(4)	0.73(6)	4.60
O1	0.1577(2)	0	0.4606(5)	1.00(6)	2.09
O2	0.1190(18)	0	0.6375(5)	1.00(6)	1.97
O3	0.4543(2)	0	0.2982(7)	1.00(6)	2.08
O4	0.8245(2)	0	0.7994(7)	1.00(6)	2.30
O5	0.4961(2)	0	0.1324(7)	1.00(6)	2.26
O6	0.8005(19)	0	0.9654(7)	1.00(6)	2.02
O7	0.4293(15)	0.7234(3)	0.4516(4)	1.00(6)	2.10
O8	0.3879(14)	0.7244(2)	0.6196(4)	1.00(6)	2.09
O9	0.2654(12)	0.7531(2)	0.7174(4)	1.00(6)	2.16
O10	0.0919(14)	0.7327(3)	0.7897(4)	1.00(6)	2.16
O11	0.2356(16)	0.7317(3)	0.8791(5)	1.00(6)	2.07
O12	0.0484(14)	0.7396(3)	0.9459(4)	1.00(6)	2.42

[a]Space group $C2/m$, a = 10.23625(14), b = 5.90149(7), *and* c = 29.9970(4) Å, β = 93.6407(11)°, V = 1808.44(4) Å^3.

Table 2. Bi−O, Ir−O, and Ir−Ir Bond Lengths for $Ba_4BiIr_3O_{12}$ at Room Temperature, As Refined against NPD (HRPD, ISIS) Data[a]

bond	distance (Å)	bond	distance (Å)
Bi1−O2	2.334(3)	Ir4−O4	1.998(3)
Bi1−O3	2.327(3)	Ir4−O5	1.979(3)
Bi1−O8 (×2)	2.305(16)	Ir4−O10 (× 2)	1.981(18)
Bi1−O9 (×2)	2.189(17)	Ir4−O11 (× 2)	2.065(18)
Bi2−O6 (×4)	2.232(2)	Ir5−O5	2.114(3)
Bi2−O12 (×4)	2.311(13)	Ir5−O6	1.979(2)
Ir1−O1 (×2)	2.061(18)	Ir5−O11 (× 2)	2.087(2)
Ir1−O7 (×4)	2.058(15)	Ir5−O12 (× 2)	1.932(16)
Ir2−O1	1.999(3)	Ir1−Ir2 (× 2)	2.651(11)
Ir2−O2	1.953(3)	Ir3−Ir4	2.512(16)
Ir2−O7 (× 2)	2.009(17)	Ir4−Ir5	2.659(18)
Ir2−O8 (× 2)	1.943(15)	selected intertrimer bonds	
Ir3−O3	1.925(3)	Ir2−Ir3(a)	5.930(17)
Ir3−O4	2.032(3)	Ir2−Ir3 (b × 2)	5.913(15)
Ir3−O9 (× 2)	2.003(16)	Ir2−Ir2 (c × 4)	5.908(18)
Ir3−O10 (× 2)	2.076(17)	Ir2−Ir2 (d × 2)	5.90149(7)

[a]Labels (a−d) of intertrimer Ir−Ir bonds refer to Figure 2.

dx.doi.org/10.1021/ic4014619 | *Inorg. Chem.* 2013, 52, 12461−12467

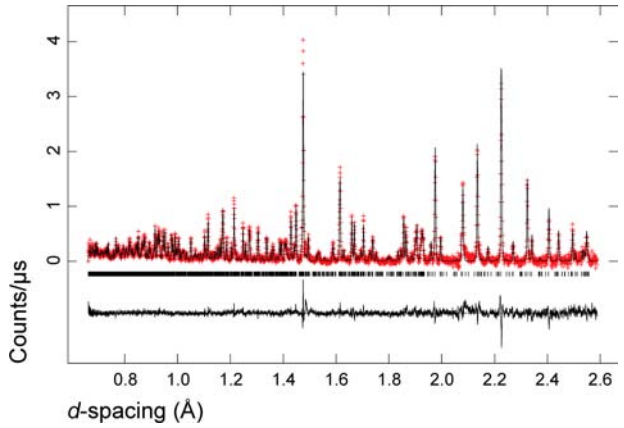

Figure 1. Observed (crosses), calculated (upper line), and difference (lower line) profiles for the final Rietveld fit of the structure of $Ba_4BiIr_3O_{12}$ to NPD data (backscattering bank of HRPD, ISIS). R_p = 0.0695, wR_p = 0.0691, χ^2 = 1.925 for 70 variables.

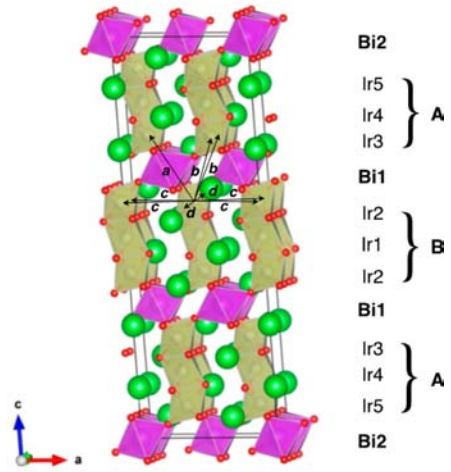

Figure 2. Room-temperature structure of $Ba_4BiIr_3O_{12}$ as refined against NPD (HRPD, ISIS) data. BiO_6 octahedra are purple, Ir_3O_{12} face-sharing trioctahedra are yellow, and Ba atoms are green. Labels on selected longer Ir–Ir distances correspond to those listed in Table 2.

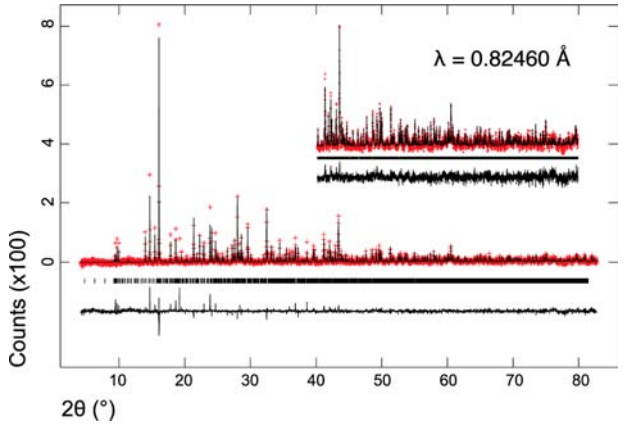

Figure 3. Observed (crosses), calculated (upper line) and difference (lower line) profiles for the final Rietveld fit to 250 K S-XRD data (PD, AS). R_p = 0.0328, wR_p = 0.0445, χ^2 = 1.828. The inset shows the high-angle region with an expanded *y*-axis.

Heat capacity (Figure 6) was measured using a relaxation technique on an approximately 10 mg sample extracted from sintered pellets.

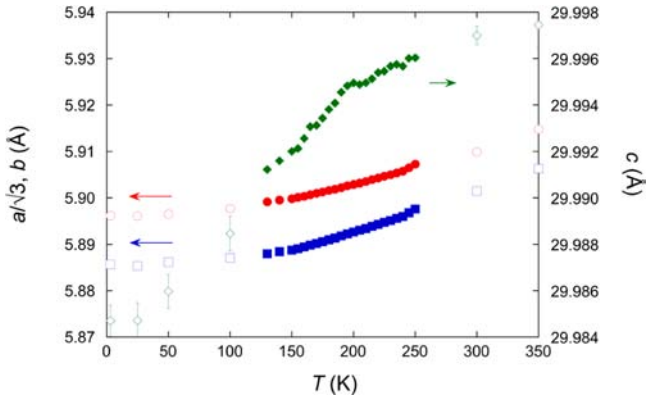

Figure 4. Temperature dependence of the lattice parameters for $Ba_4BiIr_3O_{12}$ between 3 and 350 K, from Rietveld refinement against S-XRD (closed symbols) and NPD (open symbols) data. Error bars are smaller than symbols where not shown.

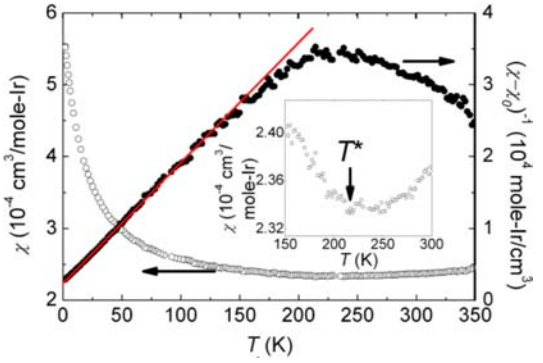

Figure 5. Temperature dependence of the molar susceptibility and its reciprocal.

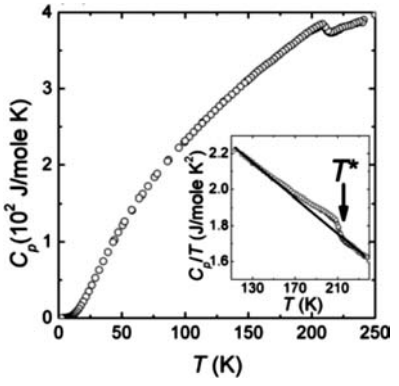

Figure 6. Temperature dependence of the specific heat, C_p.

Electrical resistivity data were collected using standard four-probe technique on the same sample that was used for heat capacity measurements.

RESULTS AND DISCUSSION

The 12L-type perovskite $Ba_4BiIr_3O_{12}$ consists of face-sharing trioctahedral Ir_3O_{12} trimers that share vertices with BiO_6 octahedra, with Ba^{2+} cations in the high-coordinate perovskite A sites. Direct Ir–Ir distances within the Ir_2O_9 trimers are relatively short at ~2.6 Å, allowing for the possibility of direct metal–metal bonding.

A comparison of the unit cell parameters across the isostructural 12L-type series $Ba_4RIr_3O_{12}$, R = lanthanoid or

dx.doi.org/10.1021/ic4014619 | Inorg. Chem. 2013, 52, 12461–12467

lanthanum[22] (Figure 7), shows that $Ba_4BiIr_3O_{12}$ has more in common with the R = Tb, Pr, and Ce compounds than with

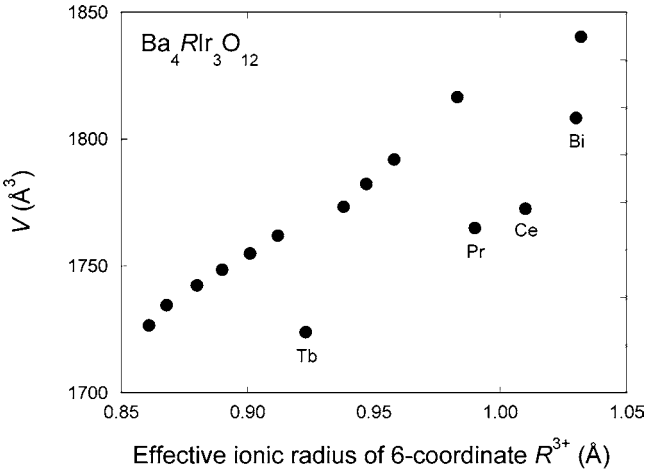

Figure 7. Effective ionic radii[29] of R^{3+} (R = Bi, Y, lanthanoid) cations in 6-fold coordination vs unit cell volume (in the equivalent *C*2/*m* cell of $Ba_4BiIr_3O_{12}$) for the 12L perovskite series $Ba_4RIr_3O_{12}$ at room temperature. Error bars are smaller than symbols. Adapted from Shimoda et al.,[22] from which all data points except R = Bi (this work) are taken.

those based on the other lanthanoids. Shimoda et al.[22] used comparisons of average R−O bond lengths to the predictions of Shannon's effective ionic radii[29] to demonstrate that the difference between the two series is due to R = Tb, Pr, and Ce adopting +4 valence states (meaning that the average valence state of Ir is also +4), whereas the other lanthanoids adopt +3 valence states (meaning that the average valence state of Ir is +4.33). In the case of $Ba_4BiIr_3O_{12}$, our data (Table 2) yield a mean Bi−O bond length of 2.27(5) Å, very close to the average (2.29 Å) of Shannon's radii for Bi^{3+} (2.43 Å) and Bi^{5+} (2.16 Å). BVS (Table 1) for the two Bi sites are calculated as 3.69 (Bi1) and 3.56 (Bi2). All these results indicate that the apparent valence state of Bi is closer to +4 than to +3. This is the same highly unusual nominal valence state for Bi that we found in $Ba_3BiIr_2O_9$[7] and $Ba_3BiRu_2O_9$.[6] Again, S-XRD and high-resolution NPD data show no evidence for symmetry lowering or short-range disorder, at any temperature, that could indicate the Bi^{3+}/Bi^{5+} disproportionation normally found in "Bi^{4+}" oxides such as $BaBiO_3$.[16] Crystallographically, therefore, $Ba_4BiIr_3O_{12}$ at room temperature is a perfect trimer analogue to the dimer compound $Ba_3BiIr_2O_9$.

Figure 4 shows the temperature dependence of the lattice parameters obtained from Rietveld refinements against S-XRD data between 150 and 250 K. A small but statistically significant anomaly is observed in the *c*-axis at the same temperature as the physical properties anomalies, reminiscent of the *c*-axis negative thermal expansion observed at *T** in $Ba_3BiIr_2O_9$.[7] However, the anomaly is far smaller: 0.003% vs 1.0% for $Ba_3BiIr_2O_9$ (or 0.3% for $Ba_3BiRu_2O_9$[6]). Similarly, magnetic susceptibility (Figure 5) and heat capacity (Figure 6) show features at ∼200 K, but they are not nearly as pronounced as for the 6H compounds. Because the standard deviations on refined bond lengths are 2 orders of magnitude larger than on lattice parameter (see Tables 1 and 2), the lattice effect cannot be unambiguously ascribed to a change in the nature of Ir−Ir bonds as for $Ba_3BiIr_2O_9$.[7] The small discrepancy between *T** observed by heat capacity vs diffraction measurements may be partly explained by the first-order nature of the transition (noting that diffraction data were collected on cooling and heat capacity data on warming). It should also be noted that the relatively coarse data collection steps in the low-temperature S-XRD measurements limit the accuracy with which *T** can be estimated. For this reason, coupled with the more accurate thermometry of the helium cryostat used for heat capacity measurements, we use the value for *T** obtained from the latter measurement in the following discussion.

Figure 5 shows the temperature dependence of the molar susceptibility χ as a function of temperature. The overall magnetic susceptibility is weakly temperature dependent, with a very shallow minimum at *T** = 215 K (see the inset). Below 150 K, the susceptibility is well described by a modified Curie−Weiss law:

$$\chi(T) = \frac{N_A g^2 \mu_B^2 J(J+1)}{3k_B(T-\theta_{CW})} + \chi_0 \quad (1)$$

where θ_{CW}, *J*, *g*, k_B, and χ_0 are the Curie−Weiss characteristic temperature, angular momentum, Landé *g*-factor, Boltzmann constant, and temperature-independent contribution to susceptibility, respectively. A least-squares fit, performed below 150 K (Figure 5), yielded an effective moment $\mu_{eff} = g\mu_B(J(J+1))^{0.5} = 0.22(2)\ \mu_B$/Ir, $\theta_{CW} = -15(1)$ K, and $\chi_0 = 2.0(2) \times 10^{-4}$ emu/mol Ir. The effective moment is much lower than the spin-only value expected for an *S* = 1/2 ion (1.73 μ_B), and much lower than value observed in $Ba_3BiIr_2O_9$ in its nondimerized state (0.9 μ_B/Ir).

Analyzing the structure of $Ba_4BiIr_3O_{12}$, we find that the exchange scheme for this compound may be complex. Because the structure consists of two crystallographically inequivalent trimers, A(Ir3−Ir4−Ir5) and B(Ir2−Ir1−Ir2), there are three possible nearest-neighbor exchanges, J_{12}, J_{34}, and J_{45}; two next-nearest neighbor exchanges within each trimer, J_{22} and J_{35}; and generalized interdimer interactions J_{AA}, J_{BB}, and J_{AB} (Figure 2). In principle, all of these interactions determine the magnetic response of $Ba_4BiIr_3O_{12}$. However, for simplicity, we will assume that the nearest-neighbor exchange dominates and may be generalized by one *J*, representing an average of J_{12}, J_{34}, and J_{45}.

Antiferromagnetic exchange within trimers of *S* = 1/2 ions should lead to different magnetic behavior in the high- and low-temperature regimes. At high temperatures, well above |*J*|, a single-ion-like response is expected due to thermal fluctuations dominating over magnetic exchange, and simple Curie−Weiss-like behavior should be observed. In the low-temperature limit, well below |*J*|, a doublet within each trimer is formed. Antiferromagnetic exchange then gives rise to a collective *S* = 1/2 configuration formed by all three moments per trimer. At temperatures comparable to |*J*|, a crossover between these two regimes should be then observed.

The experimentally observed behavior of $Ba_4BiIr_3O_{12}$ is, however, slightly different from the picture described above. Compared to 3d counterparts, magnetism in this 5d Ir^{4+} system is much weaker due to its much more extended d orbitals, causing strong hybridization with ligands and much more pronounced spin−orbit coupling.[30] This results in much lower effective moments than expected for systems where *J* is a "good" quantum number. In $Ba_4BiIr_3O_{12}$, we observe, near *T**, a transition from a weakly temperature dependent paramagnet, with a positive temperature coefficient (*T* > 220 K), to a paramagnetic region with Curie−Weiss-like magnetic suscept-

dx.doi.org/10.1021/ic4014619 | Inorg. Chem. 2013, 52, 12461−12467

ibility due to the presence of weak fluctuating magnetic moments. The values of the effective moment per Ir in $Ba_4BiIr_3O_{12}$ (0.22 μ_B/Ir) are much lower than in $Ba_3BiIr_2O_9$ (0.9 μ_B/Ir), which may indicate that in the former compound, a doublet $S = 1/2$ ground state develops below T^* within magnetic Ir_3O_{12} trimers. The slightly negative characteristic Curie–Weiss temperature $\theta_{CW} = -15$ K then reflects then weak antiferromagnetic exchange among these doublets (J_{AA}, J_{AB}, and J_{BB}).

A similar model has been proposed to describe the magnetism of $Ba_4CeIr_3O_{12}$.[25] However, no signature of a T^*-like transition was reported in that compound, and its effective moment was much closer to the theoretical value expected for a $S = 1/2$ doublet (almost 1.7 μ_B/trimer vs 0.4 μ_B/trimer for $Ba_4BiIr_3O_{12}$).

Figure 6 shows the temperature dependence of the heat capacity C_p as a function of temperature. Below $T^* \sim 215$ K, an anomaly starts to develop with a maximum at 210 K, extending down to about 150 K. As we were not able to find suitable nonmagnetic counterpart compound, we have estimated the heat capacity associated with the T^* transition on the assumption that the C_p/T associated with the crystal lattice is a linear function of T in the range 115–270 K (inset in Figure 6). The estimated entropy associated with this transition is very small: only about 1.1 J K^{-1} mol^{-1} (Ir), compared to R ln2 = 5.75 J K^{-1} mol^{-1} expected for an $S = 1/2$ system undergoing a long-range magnetic ordering transition.

Figure 8 shows the electrical resistivity as a function of temperature. The overall character of the resistivity is typical of

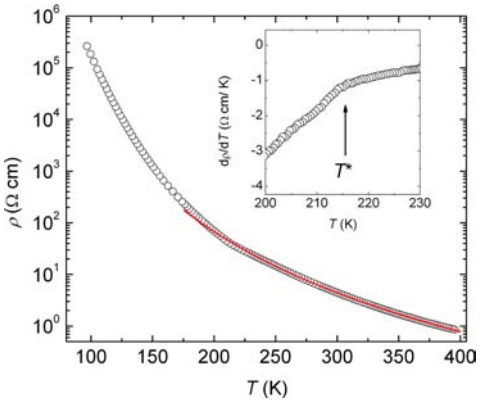

Figure 8. Temperature dependence of the electronic resistivity ρ. The solid line is a fit to eq 3. The inset shows the temperature derivative of resistivity vs temperature in the vicinity of T^*.

semiconductors, with ρ increasing as temperature decreases. The T^* transition is apparent as a kink in $\rho(T)$ and a rapid change in $d\rho/dT$ (shown in the inset). In general, the temperature dependence of the resistivity for semiconductors can be described by one of three models: an Arrhenius law, Mott's variable-range hopping expression or the nearest-neighbor hopping of small polarons. Above T^*, $\rho(T)$ is well described by the variable range hopping model:[31]

$$\log \rho = a + bT^{-1/1+n} \quad (3)$$

where a and b are model parameters and n is the effective dimensionality of hopping. This model was developed for materials where the conduction is mediated by localized states via thermally induced hopping. A least-squares fit yields $a = -8.1$, $b = 52$ Ω cm $K^{3.2}$, and $n = 2.2$. A rapid change of resistivity at T^* suggests a change in the electronic structure of $Ba_4BiIr_3O_{12}$ (i.e., an increase of the band gap or a reduction in charge-carriers concentration or mobility).

The results and analysis presented above provide new information about the character of the T^* transition in the dimer system $Ba_3BiIr_2O_9$[7] as well as in this new trimer system $Ba_4BiIr_3O_{12}$. $Ba_3BiIr_2O_9$ undergoes a pronounced magnetoelastic transition associated with opening of a gap in the spin-excitation spectrum at $T^* = 74$ K, to which the $T^* = 215$ K transition in $Ba_4BiIr_3O_{12}$ appear to be analogous. Our observations for $Ba_4BiIr_3O_{12}$ on cooling through T^* can be summarized as follows: (i) a change from non-Curie–Weiss and very weakly temperature dependent susceptibility above T^* to Curie–Weiss behavior with a low effective moment due to the formation of $S = 1/2$ trimers below T^*, (ii) a release of structural/magnetic entropy, (iii) an anomalous thermal lattice expansion, and (iv) a change in the electrical structure, apparent as an anomaly in the electrical resistivity. Taken together, these findings present a picture of a transition based on magnetocrystalline coupling between lattice and magnetic degrees of freedom. According to this model, the transition results in a gain of magnetic energy (due to the formation of antiferromagnetically coupled $S = 1/2$ trimers), which over-compensates for the loss of elastic energy arising from the structural distortion. Above T^*, magnetic susceptibility is very weakly temperature dependent with a positive temperature coefficient, suggesting that there is very strong exchange within trimers, but that $S = 1/2$ ground state doublets have not been able to form. This suppression of doublet formation above T^* could be explained by geometric frustration, due to competing antiferromagnetic exchange among the trimers.[32] Table 2 lists the intertrimer Ir–Ir distances from Ir2, the peripheral site of trimer B (see Figure 2). Because the trimers are triangularly disposed relative to each other, there are a total of 9 intertrimer Ir–Ir bonds from Ir2, all between 5.91 and 5.93 Å and therefore all closely competing. Below T^*, the frustration is overcome, producing the observed small structural anomaly in the c-axis (along which the Ir–Ir–Ir intratrimer bonds are aligned), and the moments within trimers form $S = 1/2$ doublets so that weak antiferromagnetic coupling among them starts to become apparent in magnetic susceptibility. In this model, the T^* transition is analogous to that seen in $Ba_3BiIr_2O_9$.

It should be pointed out that this model is almost certainly an oversimplification, and that there remain some experimental observations that it does not fully or satisfactorily explain. In particular, it offers no insight into the cause of the strongly reduced effective moment of 0.22(2) μ_B/Ir compared to the expected spin-only value of 1.73 μ_B/Ir despite the excellent fit to the Curie–Weiss law at low temperatures. We have therefore considered several other possible models, described below. Although these models are in fact less complete in terms of their ability to explain our data, it is possible that the true nature of $Ba_4BiIr_3O_{12}$ incorporates aspects of each.

One alternative model is that for $T > T^*$, no localized spins at all are present, resulting in an almost temperature-independent magnetic susceptibility. Below T^*, charge carriers are localized into trimers that bear local magnetic moments with doublet ground state. However, this scenario predicts a metallic state above T^*, which is contrary to our observations.

The final model that could potentially explain all experimentally observed phenomena is the onset of charge order in the form of a so-called charge density wave (CDW), a

dx.doi.org/10.1021/ic4014619 | Inorg. Chem. 2013, 52, 12461–12467

well-known precondition to high-temperature superconducting states, such as occurs in $BaBiO_3$,[33] which, like $Ba_4BiIr_3O_{12}$, contains Bi in the unusual nominal oxidation state of +4. In that compound, "Bi^{4+}" is known to disproportionate into Bi^{3+} and Bi^{5+}, and this seems to play a critical role in the CDW state. In $Ba_4BiIr_3O_{12}$ (and $Ba_3BiIr_2O_9$), the structural distortion at T^* could be a hallmark of charge ordering in Bi sublattice; however, in both cases we found no evidence for satellite reflections or lattice strain in our diffraction patterns below T^*.

CONCLUSIONS

We have synthesized the 12L hexagonal perovskite $Ba_4BiIr_3O_{12}$ for the first time by conventional solid-state reaction. This compound contains face-sharing octahedral Ir_3O_{12} trimers, related to the Ir_2O_9 dimers in the spin-gap compound $Ba_3BiIr_2O_9$, and we observe anomalies in lattice constants, magnetic susceptibility, heat capacity, and electrical resistivity in the proximity of T^* = 215 K that mirror those seen at T^* = 74 K in $Ba_3BiIr_2O_9$. By analogy to the dimer system, which shares the same electronic state of Ir and Bi, we can explain our experimental observations by the formation of S = 1/2 doublets within trimers at T^*. However, different magnetic ground states are predicted for antiferromagnetically coupled dimers (S = 0 singlet) and trimers (S = 1/2 doublet), which explains the gapless magnetic susceptibility in $Ba_4BiIr_3O_{12}$ compared to the spin-gap opening seen in $Ba_3BiIr_2O_9$. Similarly to the dimer compound, the 5d states appear to be strongly hybridized with surrounding orbitals, resulting in very low experimentally observed effective magnetic moments. Finally, although this model is internally consistent, it is most likely incomplete and does not explain all aspects of our experimental observations, notably the strongly reduced moments per Ir. Future investigations of the magnetic excitation spectrum of $Ba_4BiIr_3O_{12}$, using computational first principles methods (density functional theory) as well as experimental inelastic neutron scattering, should provide further insights into the strong coupling between magnetism and structure in these materials, leading to a more complete model for the unusual low-temperature behavior of $Ba_4BiIr_3O_{12}$.

ASSOCIATED CONTENT

Supporting Information

Crystallographic information file (CIF) for the room-temperature structure of $Ba_4BiIr_3O_{12}$ as Rietveld-refined against NPD data (HRPD, ISIS). This material is available free of charge via the Internet at http://pubs.acs.org.

AUTHOR INFORMATION

Corresponding Author

*C. D. Ling. E-mail: chris.ling@sydney.edu.au.

Present Addresses

[§]Department of Physics and Astronomy, Stony Brook University, Stony Brook, New York 11794, United States.

[⊥]Department of Chemistry, University of Cambridge, Lensfield Road, Cambridge CB2 1EW, United Kingdom.

Author Contributions

The manuscript was written through contributions of all authors. All authors have given approval to the final version of the manuscript.

Funding

This work was supported by the Australian Research Council, Discovery Projects (DP110102662), and the Australian Institute of Nuclear Science and Engineering.

Notes

The authors declare no competing financial interest.

ACKNOWLEDGMENTS

The authors thank Dr. Kevin Knight of the ISIS Facility and Dr. Qinfen Gu of the Australian Synchrotron for their assistance in the collection of time-of-flight neutron diffraction and synchrotron X-ray diffraction data respectively.

ABBREVIATIONS

ADP, atomic displacement parameter; AFM, antiferromagnetic; BVS, bond valence sums; CDW, charge-density wave; NPD, neutron powder diffraction; NTE, negative thermal expansion; S-XRD, synchrotron X-ray powder diffraction; VSM, vibrating sample magnetometer; XRD, X-ray powder diffraction

REFERENCES

(1) Tokura, Y.; Nagaosa, N. *Science* **2000**, *288*, 462.
(2) Vasil'ev, A. N.; Markina, M. M.; Popova, E. A. *Low Temp. Phys.* **2005**, *31*, 203.
(3) Oosawa, A.; Ono, T.; Tanaka, H. *Phys. Rev. B* **2002**, *66*, 020405.
(4) Nakajima, T.; Mitamura, H.; Ueda, Y. *J. Phys. Soc. Jpn.* **2006**, *75*, 054706.
(5) Radaelli, P. G.; Horibe, Y.; Gutmann, M. J.; Ishibashi, H.; Chen, C. H.; Ibberson, R. M.; Koyama, Y.; Hor, Y. S.; Kiryukhin, V.; Cheong, S. W. *Nature* **2002**, *416*, 155.
(6) Miiller, W.; Avdeev, M.; Zhou, Q.; Studer, A. J.; Kennedy, B. J.; Kearley, G. J.; Ling, C. D. *Phys. Rev. B* **2011**, *84*, 220406(R).
(7) Miiller, W.; Avdeev, M.; Zhou, Q.; Kennedy, B. J.; Sharma, N.; Kutteh, R.; Kearley, G. J.; Schmid, S.; Knight, K. S.; Blanchard, P. E. R.; Ling, C. D. *J. Am. Chem. Soc.* **2012**, *134*, 3265.
(8) Darriet, J.; Bontchev, R.; Dussarrat, C.; Weill, F.; Darriet, B. *Eur. J. Solid State Inorg. Chem.* **1993**, *30*, 273.
(9) Ling, C. D.; Kennedy, B. J.; Zhou, Q. D.; Spencer, J. R.; Avdeev, M. *J. Solid State Chem.* **2010**, *183*, 727.
(10) Doi, Y.; Hinatsu, Y. *J. Solid State Chem.* **2004**, *177*, 3239.
(11) Doi, Y.; Hinatsu, Y. *J. Phys.: Condens. Matter* **2004**, *16*, 2849.
(12) Doi, Y.; Hinatsu, Y.; Shimojo, Y.; Ishii, Y. *J. Solid State Chem.* **2001**, *161*, 113.
(13) Doi, Y.; Wakeshima, M.; Hinatsu, Y.; Tobo, A.; Ohoyama, K.; Yamaguchi, Y. *J. Mater. Chem.* **2001**, *11*, 3135.
(14) Hinatsu, Y.; Oyama, S.; Doi, Y. *Bull. Chem. Soc. Jpn.* **2004**, *77*, 1479.
(15) Balzarotti, A.; Menushenkov, A. P.; Motta, N.; Purans, J. *Solid State Commun.* **1984**, *49*, 887.
(16) Chaillout, C.; Santoro, P.; Remeika, A.; Cooper, A. S.; Espinosa, G. P.; Marezio, M. *Solid State Commun.* **1988**, *65*, 1363.
(17) Cox, D. E.; Sleight, A. W. *Solid State Commun.* **1976**, *19*, 969.
(18) Flavell, W. R.; Mian, M.; Roberts, A. J.; Howlett, J. F.; Sarker, M. M.; Wincott, P. L.; Bilsborrow, R. L.; vanDorssen, G. *J. Mater. Chem.* **1997**, *7*, 357.
(19) Thornton, G.; Jacobson, A. J. *Acta Crystallogr., Sect. B: Struct. Sci.* **1978**, *34*, 351.
(20) Zhou, Q. D.; Kennedy, B. J. *Solid State Commun.* **2004**, *132*, 389.
(21) Shimoda, Y.; Doi, Y.; Hinatsu, Y.; Ohoyama, K. *Chem. Mater.* **2008**, *20*, 4512.
(22) Shimoda, Y.; Doi, Y.; Wakeshima, M.; Hinatsu, Y. *J. Solid State Chem.* **2009**, *182*, 2873.
(23) Shimoda, Y.; Doi, Y.; Wakeshima, M.; Hinatsu, Y. *Inorg. Chem.* **2009**, *48*, 9952.
(24) Shimoda, Y.; Doi, Y.; Wakeshima, M.; Hinatsu, Y. *J. Solid State Chem.* **2010**, *183*, 33.

(25) Shimoda, Y.; Doi, Y.; Wakeshima, M.; Hinatsu, Y. *J. Solid State Chem.* **2010**, *183*, 1962.
(26) Larson, A. C.; Von Dreele, R. B. GSAS: General Structure Analysis System; *LAUR 86-748*; Los Alamos National Laboratory: Los Alamos, NM, 1994.
(27) Toby, B. H. *J. Appl. Crystallogr.* **2001**, *34*, 210.
(28) Brese, N. E.; O'Keeffe, M. *Acta Crystallogr., Sect. B: Struct. Sci.* **1991**, *47*, 192.
(29) Shannon, R. D. *Acta Crystallogr., Sect. A: Cryst. Phys., Diffr., Theor. Gen. Crystallogr.* **1976**, *32*, 751.
(30) Ye, F.; Chi, S.; Chakoumakos, B. C.; Fernandez-Baca, J. A.; Qi, T.; Cao, G. *Phys. Rev. B* **2013**, *87*, 140406.
(31) Mott, N. F.; Davis, E. A. *Electronic processes in non-crystalline materials*; Clarendon Press, Oxford University Press: Oxford, U.K., 1971.
(32) Sano, K.; Takano, K. *J. Phys. Soc. Jpn.* **2000**, *69*, 2710.
(33) Mattheiss, L. F.; Gyorgy, E. M.; Johnson, D. W., Jr. *Phys. Rev. B* **1988**, *37*, 3745.